Natural Hazards
https://doi.org/10.1007/s11069-025-07186-3

ORIGINAL PAPER

Exploring the impact of rainfall temporal distribution and critical durations on flood hazard modeling

Marcus N. Gomes Jr.[1,2,3] · **Vijay Jalihal**[4] · **Maria Castro**[3] · **Eduardo M. Mendiondo**[3]

Received: 24 June 2024 / Accepted: 14 February 2025

Abstract
Flood modeling is influenced by uncertainties from factors like soil infiltration characteristics, floodplain roughness, and spatio-temporal variations in rainfall volume, distribution, and intensities. Although multiple uncertain sources arise in flood modeling, the detailed evaluation of rainfall characteristics in flood mapping is not fully investigated. This paper addresses the role of rainfall temporal distribution on flood mapping by introducing a methodology that contrasts standard synthetic design storms and compares them to the 50th percentile rainfall temporal distribution derived from high-resolution 15-min observed rainfall data. The Alternating Blocks and the Huff rainfall temporal distribution methods were chosen as representative synthetic rainfall methods for flood mapping assessment. The framework was applied in a 131 km^2 urban catchment in Bangalore, India. Evaluation of different rainfall temporal distributions reveals a potential 50% smaller areas with flood hazard, for the same return period and duration, simply by selecting a specific rainfall temporal that is not the critical for the catchment. This research not only underscores the importance of the effect of rainfall temporal distribution selection and assessment of the critical rainfall duration but also highlights the need for accurate data-driven methodologies in flood mapping, particularly in the face of urbanization and climate-induced complexities.

Keywords Flood mapping · Huff curves · Alternated blocks method · Rainfall temporal distribution · Flood hazard

1 Introduction

Urban flood inundation mapping is affected by many hydrological phenomena varying from the rainfall dynamics to the non-linear spatio-temporal representation of infiltration (Cheng et al 2020). Typically, the use of so-called event-based design storms is a common engineering practice to delineate flood-prone areas (Mei et al 2020; Kang et al 2013), especially when high-resolution quality data of rainfall is lacking (Gomes et al 2023). Multiple areas across the world use the 100-yr return period as the common return period used to define flood-risk areas (Huang and Wang 2020; Dottori et al 2022), although the definition of the rainfall duration and temporal distribution are hardly ever specified (Krvavica and Rubinić 2020).

Extended author information available on the last page of the article

The importance of flood modeling and mapping associated with rainfall return periods is evident for instances such as aiding in the development of flood insurance plans (Mani et al 2014) or even by being used to define multifaceted risk areas that would depend not only on hydrological but also socioeconomic information (Roldán-Valcarce et al 2023; Pregnolato et al 2024; Zare et al 2024). Even though multiple applications use products derived from flood simulation results, a large uncertainty can arise from not clearly defining the rainfall's duration and temporal distribution that would maximize the expected flood hazard (e.g., maximum water depth).

Two storms with the same return period can have dramatically different catchment responses simply by varying the temporal rainfall distribution and/or the rainfall duration. We hypothesize that these rainfall characteristics must be properly defined, investigating the critical rainfall duration that maximizes a spatial flood hazard criterion. Flood hazard can be defined as a function of various features, such as the floodplain area with significant flood depth, velocity, or ultimately, areas with human instability hazards (Lazzarin et al 2024). The latter can be estimated via flood momentum equations and dynamic friction modeling (Jonkman and Penning-Rowsell 2008) or mixed deterministic-probabilistic approaches as presented in Lazzarin et al (2022).

The commonly accepted definition of critical rainfall duration is based on the duration leading to the maximum outflow peak (Krvavica and Rubinić 2020). However, this definition may not align with other critical flood hazard metrics, such as maximizing areas prone to human instability or those with substantial flood depth. Additionally, there is a lack of consensus on widely accepted rainfall temporal distribution and duration, with many engineering design studies arbitrarily selecting these rainfall characteristics (Krvavica and Rubinić 2020).

This paper defines a systematic heuristic method using a 2D hydrologic-hydrodynamic modeling approach to estimate the critical rainfall duration that maximizes flood hazard indicators such as floodplain extent, areas with relatively high velocities, and areas with human instability hazards. The methods developed in this paper are tested in a real-world catchment in Bangalore, India.

Challenges in sub-daily rainfall data are primarily rooted in the scarcity of prolonged, reliable records encompassing extreme rainfall events at shorter time scales (Westra et al 2014). Key impediments include the lack of comprehensive global repositories for sub-daily data, limitations in instruments measuring short yet intense rainfall, evolving technological incompatibilities, and variations in quality assessment methods. These challenges hinder our capacity to ascertain whether extreme sub-daily rainfall is increasing due to climate change and subsequently impact our understanding of whether flood hazard frequencies align with rainfall trends.

Flood hydrologic response is influenced by the spatio-temporal variability in rainfall (Zhu et al 2018; Chen et al 2023). The study conducted by Breinl et al (2021) found that regions with convective rain patterns exhibit increased variability in extreme rainfall, whereas orographic rain regions display greater variability in streamflow runoff. In essence, the research suggests that the characteristics of rainfall intensity, duration, frequency, and streamflow runoff are influenced by factors including spatial distribution of rain, geological features, and soil storage capacity. In the same direction, the research carried out in Cristiano et al (2017) emphasizes the intricate spatial and temporal variability characterizing hydrological processes within urban environments. This variability is particularly heightened by the influence of impervious surfaces and the diverse land use patterns present that influence the flow dynamics within urban catchments.

The investigation conducted by Bezak et al (2018) exposes the reliance of critical rainfall duration, particularly in maximizing peak flows within Huff curves (Huff 1967), on the catchment time of concentration. Nevertheless, they emphasize the lack of a universally defined method within the engineering community to estimate this critical duration. Furthermore, Bezak et al (2018) notes that prolonging rainfall duration amplifies disparities in peak discharge and time-to-peak. Scenarios featuring extended rainfall durations while adhering to the same Huff curve yield smaller peak discharge values compared to cases where rainfall duration closely matches the catchment time of concentration. The study indicates that more research is required to understand critical rainfall duration.

Many studies aimed at determining critical duration primarily concentrate on identifying the duration that maximizes flood hazard, often focusing on catchment-integrated hydrological sub-products, particularly the maximum peak flow (Yuan et al 2021; Bezak et al 2018). While the maximum peak flow is connected to flood characteristics, its limitation is neglecting the impact on floodplain extent, especially in smaller urbanized areas with diverse land use patterns contributing to nonlinear runoff. This highlights the need for a spatialized metric to define critical rainfall duration and temporal distribution, specifically emphasizing maximizing considerations for spatial flood hazard assessment.

With urban floods posing many challenges to city dwellers and planners, several spatial and temporal hydrological models were developed so that authorities could make better decisions in flood prevention and risk management. Models using Stormwater Management Model (SWMM) (Rossman 2010), machine learning techniques (Mosavi et al 2018), neural networks (do Lago et al 2023), and physically-based fully distributed models (Gomes et al 2023) are some of the solutions being developed by the research community all over the world to analyze, predict and control flood risks enabling the decision-makers and city authorities to formulate a plan to improve the infrastructural conditions (Teng et al 2017).

Flood or hydrodynamic modeling can be uncertain and difficult in data-scarce areas and scenarios. However, these areas are generally the areas with relatively higher exposure and vulnerability of the population (Batalini de Macedo et al 2022; Membele et al 2022). An example of such cases is the floods in Bellandur, a very urbanized catchment in Bangalore, India. Although we apply our methods in this catchment, we attempt to develop a case-study-free analysis that uses only freely available datasets and can be adapted to poorly gauged catchments and catchments with more climatologic-hydrologic data.

While recent literature offers diverse tools for flood hazard modeling and mitigation, the absence of proper high-resolution rainfall and terrain data remains challenging for assessing floods in poorly gauged watersheds. Despite data limitations, developing a method that provides meaningful results for flood hazards in these areas is relevant for decision-makers. Additionally, there is no consensus on using synthetic design storms, rainfall durations, and return periods critical for flood inundation mapping and modeling. Moreover, there is a gap in research investigating the impact of rainfall duration and temporal distribution on human instability hazards. We address these issues by presenting a flood hazard zoning method that evaluates varied rainfall durations and temporal distributions.

Our ultimate goal is not to provide a definitive solution for determining the duration times and temporal distributions of critical rainfall regarding flood hazard. These are closely related to catchment and climate signatures. Instead, we seek to elucidate the impact of neglecting these catchment-specific characteristics and their potential effects in flood hazard modeling. The fundamental contributions of this paper are:

- We develop a flood mapping framework for relatively small, poorly-gauged catchments using a 2D hydrodynamic modeling approach that requires catchment GIS data and a rainfall intensity-duration-frequency (IDF) curve. Spatial parameters can be assigned in tables according to land use and soil classifications. Therefore, this framework can be used to generate first-order site-specific catchment information, such as flood mapping and areas with human instability.
- We evaluate the effects of the rainfall duration and temporal distribution on the modeling assessment of water depths, velocities, human instability, and infiltrated depths, providing a comprehensive analysis of the effects of not choosing a critical rainfall duration and temporal distribution.
- We evaluate flood mapping characteristics under uncertainty scenarios of rainfall temporal distribution using the Alternated Blocks Method, Huff, and Observed hyetographs under 2, 6, 12, 24, and 48 h rainfall durations. The analysis is performed for flood depths, flood velocities, human instability index, and infiltration depths.

2 Material and methods

2.1 Mathematical model

HydroPol2D, as detailed by Gomes et al (2023), is a comprehensive hydrological-hydrodynamic and transport and fate model. It employs the Green-Ampt equation (Green and Ampt 1911) for estimating hortonian overland flow. The current version accounts for kinematic wave, local-inertial, and diffusive-like shallow water equation solvers to propagate excess of infiltration generated in the hydrological module (Gomes Jr et al 2024).

2.1.1 Conservation of mass and momentum

The elementwise cell-by-cell mass balance equation computes the interaction among atmospheric boundary conditions, infiltration losses, flood routing and can be written as follows:

$$d_{i,j}^{t+\Delta t} = d_{i,j}^{t} + \Delta t\left[\sum_{\mathcal{N}_{i,j}} I_{i,j}^{t} - \sum_{\mathcal{N}_{i,j}} O_{i,j}^{t} + r_{i,j}^{t} - f_{i,j}^{t}\left(d_{i,j}^{t}, F_{i,j}^{t}\right) - e_{i,j}^{t}\right], \tag{1}$$

where t is the time [T], d is the water depth [L], Δt is the time-step [T], I is the inflow rate [$L \cdot T^{-1}$], O is the outflow rate [$L \cdot T^{-1}$], r is the rainfall rate [$L \cdot T^{-1}$], f is the infiltration rate [$L \cdot T^{-1}$], F is the cumulative infiltration depth [L], e is the real evapotranspiration [$L \cdot T^{-1}$], and $\mathcal{N}$ represents the domain subset of all neighbors of cell i, j (Gomes et al 2023).

The flux term ($\sum_{\mathcal{N}_{i,j}} I_{i,j} - \sum_{\mathcal{N}_{i,j}} O_{i,j}$) is approximated at the cell edge with a momentum equation, solved for each cartesian direction in the watershe domain.

Let us drop the subindex $i + 1/2$ to represent the cell edge at the x cartesian axis (Gomes Jr et al 2024). By assuming a local-inertial approximation in the momentum equation via a s-centered scheme (De Almeida and Bates 2013), we can consider that:

$$q^{t+\Delta t} = \frac{\theta^t q^t + (1-\theta^t)\left(\frac{q^t_{i+3/2,j}+q^t_{i-1/2,j}}{2}\right) - g\hat{d}^t \Delta t S^t}{\left(1 + g\Delta t n^2 |q^t_{i+1/2}| / \hat{d}^{t7/3}\right)}, \tag{2}$$

where $q = Q/\Delta x$ is the flow per unit width [$\mathrm{L} \cdot \mathrm{T}^{-1}$], Δx is the grid resolution [L], θ is a diffusivity weighting factor [−], S is the water surface elevation slope [−], n is the Manning's roughness coefficient [$\mathrm{T} \cdot \mathrm{L}^{-1/3}$], and $\hat{d}$ is the effective water surface depth at the cell edge [L] following De Almeida and Bates (2013). All calculations of flows are made to the cell edges. Index i represents the center of the i-th cell, and the previous equation is solved twice per cell for each cartesian axis at the cell edges $(i + 1/2)$ and $(j + 1/2)$. For simplicity, only equations for the x (i.e., edge $i + 1/2$) axis are shown.

The diffusion weight factor controls the amount of diffusivity from neighbor cells at cell interfaces and is given by (Sridharan et al 2020):

$$\theta^t = 1 - \frac{\Delta t}{\Delta x} \min\left(\frac{|q^t|}{\bar{d}^t}, \sqrt{g\hat{d}^t}\right). \tag{3}$$

Using the states modeled by HydroPol2D, it is possible to determine drag forces and to calculate the human instability risk due to friction.

2.2 Time-stepping

An adaptive time-stepping scheme is implemented in HydroPol2D considering the wave celerity propagation, given by (Bates et al 2010):

$$\Delta t^t = \min\left(\alpha \frac{\Delta x}{\sqrt{g d^t}}\right), \tag{4}$$

where α is typically assumed between 0.4 and 0.7 (De Almeida and Bates 2013) and is assumed as 0.5 in this paper. The previous equation is solved for each active domain cell.

2.3 Hydrologic modeling

HydroPol2D accounts for infiltration modeling via either explicit or implicit Green-Ampt schemes, depending on user defined parametrization. In this paper, we solve the implicit GA equation using the Newton–Raphson algorithm. The implicit Green-Ampt formulation is given by (Rossman 2010):

$$F^{t+\Delta t} = K_s \Delta t + F^t + \psi_f \theta_d \left[\log\left(F^{t+\Delta t} + \psi_f \theta_d\right) - \log\left(F^t + \psi_f \theta_d\right)\right] - f_{\text{out}}, \tag{5}$$

where K_s is the saturated hydraulic conductivity [$\mathrm{L} \cdot \mathrm{T}^{-1}$], F is the infiltrated depth [L], θ_d is the effective porosity [$\mathrm{L}^3 \cdot \mathrm{L}^{-3}$], ψ_f is the wetting front suction head [L], and f_{out} is the groundwater replenishing rate, following Huber et al (2005).

The infiltration rate f is calculated by:

$$f^{t+\Delta t} = \frac{F^{t+\Delta t} - F^t}{\Delta t}, \tag{6}$$

and is used in Eq. (1) to solve the mass balance and later to propagate the flow.

2.3.1 Human instability modeling

During flood events, effects of sliding and toppling can occur depending on the velocities and water depth magnitudes (Kvočka et al 2016). In this paper, we estimate the occurrence of these effects by calculating the forces associated with the flow following the methodology proposed in Jonkman and Penning-Rowsell (2008). Sliding instability occurs when the available static friction (i.e., calculated using the difference between the weight of a person and its buoyancy) is smaller or equal to the hydrodynamic force associated with the perpendicular flow (Jonkman and Penning-Rowsell 2008). The governing equations to calculate the human instability hazard (f_r), depends on the person's volume (Eq. (7a)), weight (Eq. (7b)), drag force (Eq. (7c)), buoyancy (Eq. (7d)), and friction resistance (Eq. (7e)) and are accounted to determine f_r. Considering a cell (i, j) in the domain, these functions are written, respectively, as follows:

$$V_c = L_p B_p d \tag{7a}$$

$$F_p = mg \tag{7b}$$

$$F_q = \frac{1}{2}\rho C_d B_p d v^2 \tag{7c}$$

$$F_b = \rho V_c g \tag{7d}$$

$$F_f = \mu\left(F_p - F_b\right) \tag{7e}$$

$$f_r = \min\left(\frac{F_q}{F_f}, 1\right), \tag{7f}$$

where the subscripts p, q, b, and f represents person, flow, buyoance, and friction. The person's height, length, and width are given by H_p, L_p, and B_p [L]. Parameters g, C_d, μ are the gravity acceleration [$L \cdot T^{-2}$], the drag coefficient [-], the kinematic static factor [-]. The water density is given by ρ [$M \cdot L^{-3}$]. The product Bd represents the person area perpendicular to the flow direction. A value of $f_r = 1$ represents that a person would be dragged in the water due to sliding instability.

The previous set of equations (7) are solved for each computational time-step, and after the end of the simulation, the time-dependent maps of f_r are plotted, as well as the maximum values of f_r per cell that would define the human instability flood hazard map. For the sake of parsimony, we assumed $u = 0.5$, $m = 75$ kg, $C_d = 1.1$, $\rho_p = 1000$ kg $\cdot$ m^{-3}, $H_p = 1.75$ m, $L_p = 0.3$ m, $B_p = 0.3$ m, and $g = 9.81$ m $\cdot$ s^{-2}.

2.4 Design hyetographs

The intensity-duration-frequency curve is given by a Sherman type, such that:

$$i = \frac{K\mathrm{RP}^{a}}{(b + t_{\mathrm{d}})^{c}}, \tag{8}$$

where K, a, b, and c are fitted parameters using a theoretical distribution frequency curve (e.g., Gumbel), and RP is the return period.

2.4.1 ABM - chicago hyetograph

The method assumes that the rainfall volume obtained by the IDF curve distributes following a peak factor γ, such that if $\gamma = 0.5$, the maximum intensity value of rainfall would be centered. The Chicago method hence equals the ABM if $\gamma = 0.5$ (Gomes Jr et al 2023).

$$i(t) = \frac{K \times \mathrm{RP}^{a}\left[\frac{t_1}{\gamma}(1-c)+b\right]}{\left(\frac{t_1}{\gamma}+b\right)^{1+c}} \text{ for } t = t_1 \le \gamma \times t_{\mathrm{d}} \tag{9a}$$

$$i(t) = \frac{K \times \mathrm{RP}^{a}\left[\frac{t_2}{\gamma}(1-c)+b\right]}{\left(\frac{t_2}{1-\gamma}+b\right)^{1+c}} \text{ for } t = t_2 > \gamma \times t_{\mathrm{d}}, \tag{9b}$$

where γ is a peak factor assumed as 0.5 to represent the rainfall peak at 50% of the storm duration and Eqs. (9a) and (9b) represent equations for durations before peak and after peak.

2.4.2 Huff hyetographs

The polynomial equations used in the model to represent the Huff temporal distribution are presented as follows (Gomes Jr et al 2023):

$$P(t)/P_t = 0.2558\left(\frac{t}{t_{\mathrm{d}}}\right)^{4} + 1.5586\left(\frac{t}{t_{\mathrm{d}}}\right)^{3} - 4.346\left(\frac{t}{t_{\mathrm{d}}}\right)^{2} + 3.603\left(\frac{t}{t_{\mathrm{d}}}\right) - 0.0579, \text{ For } t \le 2\mathrm{h} \tag{10a}$$

$$P(t)/P_t = 6.1888\left(\frac{t}{t_{\mathrm{d}}}\right)^{4} - 14.996\left(\frac{t}{t_{\mathrm{d}}}\right)^{3} + 10.861\left(\frac{t}{t_{\mathrm{d}}}\right)^{2} - 1.0758\left(\frac{t}{t_{\mathrm{d}}}\right) + 0.0235, \text{ For } 2\mathrm{h} \le t \le 12\mathrm{h} \tag{10b}$$

$$P(t)/P_t = 71.986\left(\frac{t}{t_{\mathrm{d}}}\right)^{6} + 206.68\left(\frac{t}{t_{\mathrm{d}}}\right)^{5} - 211.78\left(\frac{t}{t_{\mathrm{d}}}\right)^{4} - 92.488\left(\frac{t}{t_{\mathrm{d}}}\right)^{3} + 16.973\left(\frac{t}{t_{\mathrm{d}}}\right)^{2} - 0.5697\left(\frac{t}{t_{\mathrm{d}}}\right) + 0.0041, \text{ For } 12\mathrm{h} \le t \le 24\mathrm{h} \tag{10c}$$

$$P(t)/P_t = -58.036\left(\frac{t}{t_{\mathrm{d}}}\right)^{6} + 154.96\left(\frac{t}{t_{\mathrm{d}}}\right)^{5} - 151.59\left(\frac{t}{t_{\mathrm{d}}}\right)^{4} + 68.269\left(\frac{t}{t_{\mathrm{d}}}\right)^{3} - 13.978\left(\frac{t}{t_{\mathrm{d}}}\right)^{2} + 1.3842\left(\frac{t}{t_{\mathrm{d}}}\right) - 0.008, \text{ For } t \ge 24\mathrm{h}, \tag{10d}$$

where Eqs (10a), (10b), (10c), and (10d) represent polynomial equations for Huff's 1st, 2nd, 3rd, and 4th quartiles, respectively. Variables t and t_d are the time and the rainfall duration. $P(t)$ is the cumulative rainfall volume at time t [L] and P_t is the total rainfall volume [L].

2.5 Case study

Floods are one of the deadliest natural disasters, and India is a country prone to floods that affect ecosystems and infrastructure and lead to casualties (De et al 2013; Avinash 2013). India has a diverse topography and rich natural bio-diversity ranging from deserts to glacial mountain regions. It is the 7th largest country by size and one of the most populous countries in the world with over 1.4 billion people according to United Nations Population Prospects(2022) estimates (Nations 2022) and is expected to surpass the 1.5 billion mark by 2025 and surpass China within a decade (Kc et al 2018). With this increase in population and economic growth over the last few decades, India saw an increase in urbanization as the rural population began to migrate to cities for better employment opportunities and a better standard of living (Bhagat 2011).

Bangalore is located at 12°59' north latitude and 77°57' east longitude, almost equidistant from the eastern and western coasts of the South Indian peninsula. It is situated at an altitude of 920 m above mean sea level (MSL) with an area of 741 km^2. The mean annual total rainfall is about 900 mm (Ramachandra and Aithal 2019). The summer temperature ranges from 18 to 38°C, while the winter temperature ranges from 12 to 25°C. Bangalore is also India's third most populous city, with a population of more than 8.5 million and a metropolitan population of 11 million as of the 2011 Census (Avinash et al 2018).

The city's topography is over a natural ridge delineating four major watersheds. Hebbal, Koramangala, Challaghatta, and Vrishabhavathi valleys pass from the city's ridge in the north to an enclosed lake system at the perimeter of Bangalore. Waterbodies are part of these four major waterways, or "valley" systems, which drain most of the city's stormwater to large tanks or lakes traditionally used for recreation and water supply for irrigation.

These waterways, with interconnected lakes and their primary function as flood carriers, have provided the city with reasonable ecological and recreational values. The urban growth in recent times, not guided by strong strategic planning or development control measures to minimize the impacts on existing infrastructure, the surrounding environment, and the stormwater system, had severe impacts on waterways. This has led to the depletion of waterways and pollution and wastewater discharge to the stormwater system (Ramachandra and Mujumdar 2009).

Due to the size of the Bangalore stormwater system, we concentrate our study on the Bellandur Watershed (see Fig. 1), which is located in the Koramangala-Challagatta valley (K&C Valley), lies between longitude 77°39' W - 77°40' E and latitude 12°60' N - 12°50' S (Chandrashekar et al 2003) with an area of approximately 131 km^2.

The description of the rainfall data acquisition and rainfall temporal distribution methods of the Alternated Blocks Methods (Gomes Jr et al 2023) and Huff Curves (Huff 1967) is presented in the Supplementary Material. The Huff curves were derived from the original data presented in Huff (1967) by fitting a 6th-order polynomial equation.

2.5.1 DEM and land use land cover treatment

The DEM was converted into a digital terrain model (DTM) using the DTM-Filter tool followed by the SAGA close gaps function, (Conrad et al 2015), such that areas with slope

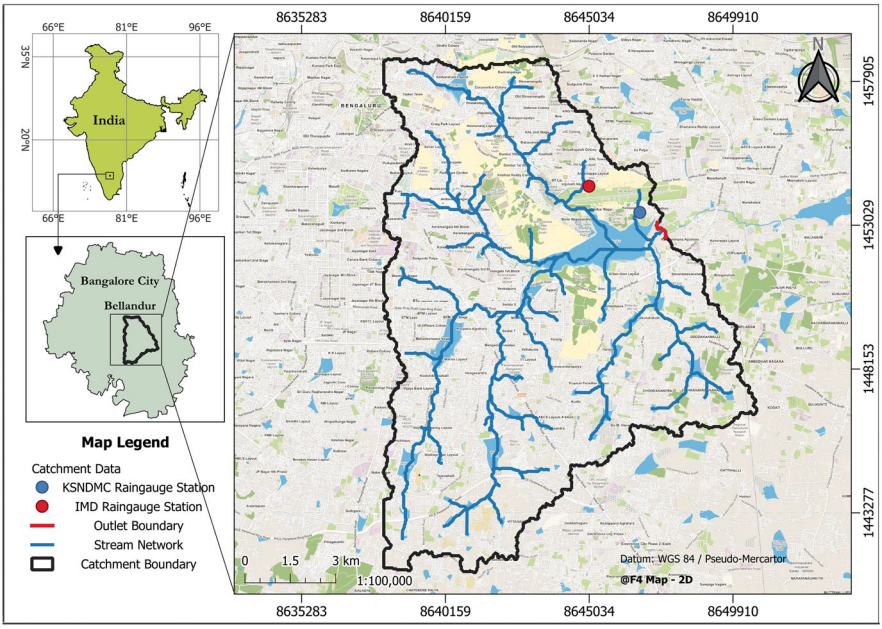

Fig. 1 Bellandur Watershed study area. The IMD Raingauge Station has daily rainfall recordings and was used to derive the IDF curve, whereas the KSNDMC Raingauge station records 15-minute rainfall and was used to derive rainfall temporal distribution patterns in the catchment

greater than 30% are bilinear interpolated, resulting in a smoother DEM. The spatial resolution of the DTM and the other rasters are 30 m for x and y directions, resulting in 145,556 squared computational cells. In addition, flow paths were smoothed using the constrained regularized smoothing (CRS) (Schwanghart and Scherler 2014). This algorithm calculates the DEM streams with a user-defined flow accumulation threshold (e.g., herein, we assume streams start at 0.5 km^2) and smooths paths, reducing DEM noises and enhancing flow continuity. Furthermore, we reduce DEM elevations in streams in terms of the flow accumulation following an exponential relationship between DEM reduction and flow accumulation (De Paiva et al 2013). These DEM treatments allow smoother rain-on-the-grid 2D simulation in the catchment domain, reducing model instabilities due to sharp slopes.

The Land Use and Land Cover (LULC) dataset from Dynamic World (Brown et al 2022), delineating nine distinct LULC types, was utilized for the temporal range period from January 1, 2021, to January 1, 2022, to generate the LULC for the watershed in this study. The DEM and the LULC maps are shown in Fig. 2.

2.5.2 Observed rainfall temporal distribution

Using the only available 6 years of 15-min resolution rainfall data retrieved from India Meteorological Department(IMD) and Karnataka State Natural Disaster Monitoring Centre (KSNDMC), we derive empirical Huff curves from the observed data to determine the rainfall temporal distribution of the catchment.

Using the time series of all events within each quartile, normalized by their durations and volumes, a Piecewise Cubic Hermite Interpolating Polynomial (PCHIP) is applied to

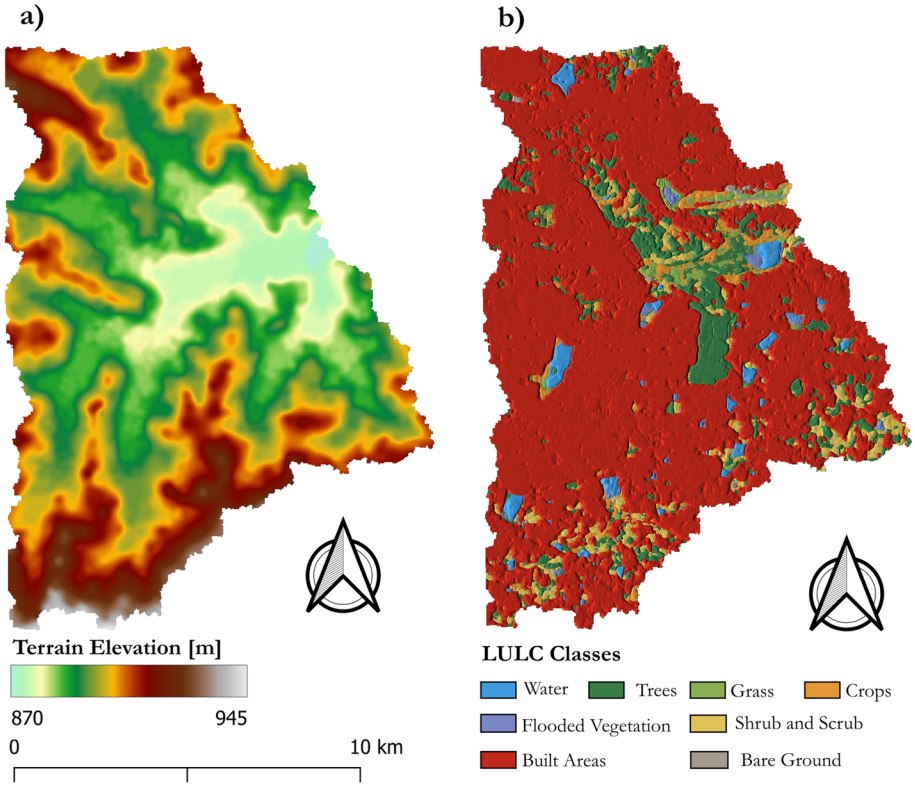

Fig. 2 **a** Digital Terrain Model (DTM) and **b** Land Use and Land Cover classification from the Dynamic World (Brown et al 2022) (LULC)

the time series at various values of t/t_d. Percentile values are then determined for probabilities of 10%, 20%, 30%, 40%, 50%, 60%, 70%, 80%, and 90%, following the methodology described by Huff (1967). Subsequently, seventh-order polynomials are fitted to these percentile curves, thereby defining the copula-based rainfall distribution functions for each probability level.

The Huff copula distributions polynomial fitting can be written as:

$$P_k/P_t = \sum_{k=1}^{n+1}\left[c_k\left(t_k/t_d\right)^{(n-k+1)}\right], \tag{11}$$

where n is the polynomial order of the Huff Curves, and k is the order of the exponent.

The coefficients c_k of Eq. (11) are obtained via least square fitting with the series of normalized time (t/t_d) versus normalized cumulative precipitation (P/P_t), for each duration tested. Rainfall events are classified into 1st, 2nd, 3rd, and 4th quartile according to the duration where the maximum intensity occurs.

Table 1 LULC-based parameters, where n is the Manning's roughness coefficient and h_0 is the initial abstraction or depression storage

LULC classification	Index	n [s · m$^{-1/3}$]	h_0 [mm]
Water	0	0.025	0
Trees	1	0.035	8
Grass	2	0.030	2
Flooded vegetation	3	0.040	4
Crops	4	0.035	5
Shrub and scrub	5	0.045	5
Built areas	6	0.025	0
Bare ground	7	0.028	0.5

2.5.3 Model parameters and initial inputs

HydroPol2D assigns hydrodynamic, hydrologic, and water quality parameters to all domain cells according to LULC and SOIL maps. The parameters used in the model are shown in Table 1 and were estimated based on data from the literature (Te Chow 1959; Rossman 2010). There is only one soil type in the catchment, and the Green-ampt parameters of saturated hydraulic conductivity (k_{sat} = 5 mm · h^{-1}), moisture deficit ($\Delta\theta$ = 0.427),

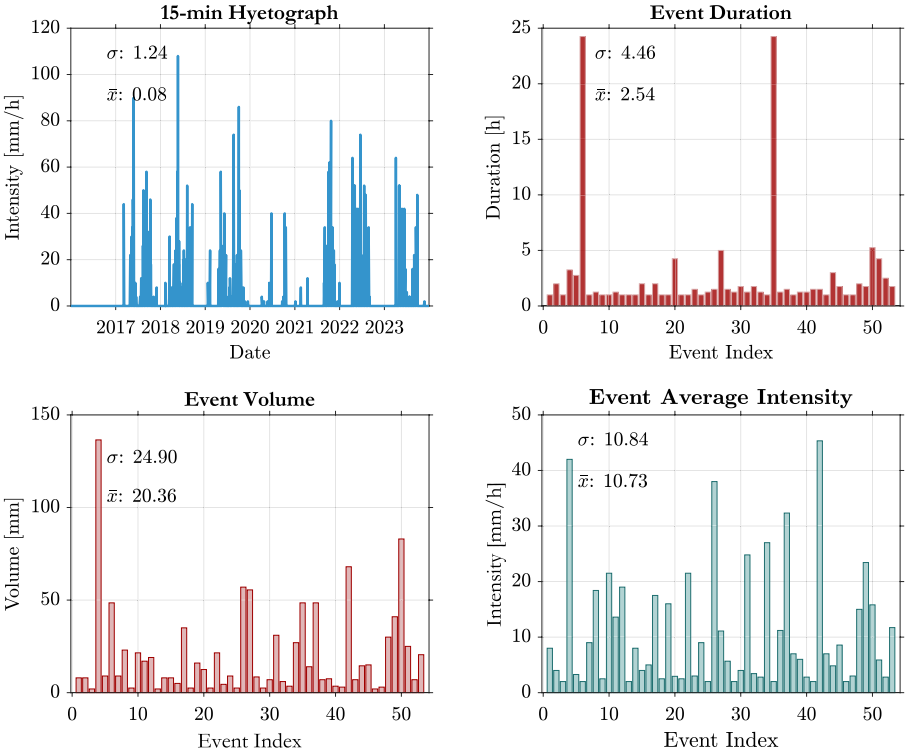

Fig. 3 Sample statistics considering a rainfall volume threshold of 0.5 mm, 6-h inter-event duration, which defined 53 events in the course of 6 years. Variables σ and $\bar{x}$ represent the standard deviation and mean of the sample

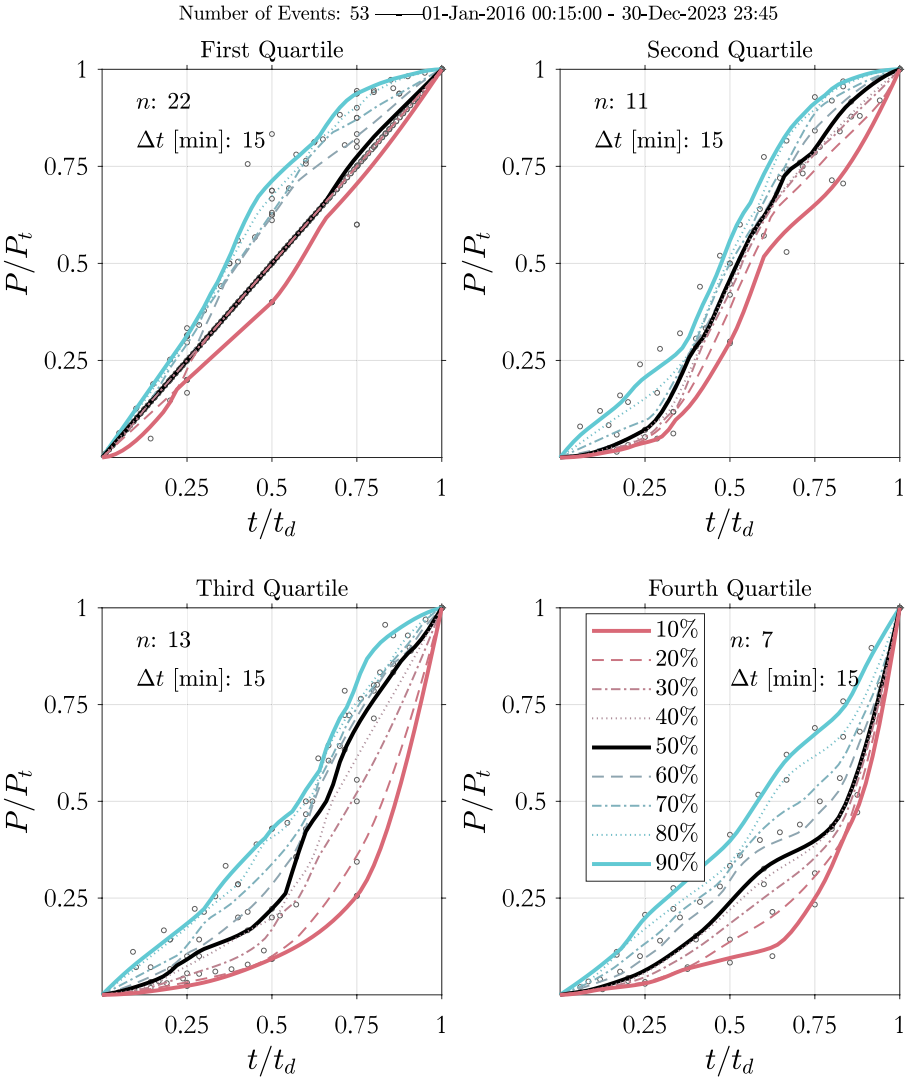

Fig. 4 Observed Huff Curves based on 6-years of 15-min rainfall, where dots are observed values and lines are fitted 7-th order polynomials interpolated with 2% increments in t/t_d. In this figure, n represents the number of events sampled, and Δt is the rainfall temporal resolution. The 7-th order polynomials fitted from the observed data are shown in the Supplemental Material

and suction head ($\psi = 40$ mm) (Brunner 2016). Another degree of freedom in the analysis could be explored by the initial soil moisture content (Pena et al 2023); however, the influence of this watershed condition is out of the scope of the paper. The initial soil moisture condition represented by the initial soil moisture depth was assumed as 10 mm for all pervious cells.

To evaluate the possible uncertainties in the parameter estimations, we perform a one-at-a-time sensitivity analysis of the model's hydrologic and hydrodynamic parameters to identify potential variations in flooded areas and areas with human instability hazards.

2.5.4 Observed copula huff curves

Data-driven rainfall temporal distribution can be derived by separating independent rainfall events according to rainfall volume and inter-event duration (Restrepo-Posada and Eagleson 1982). Normalizations from the total precipitation and total duration are performed, allowing a comparison between storm events with different characteristics. These storm events can also be classified according to the maximum volumes per quartile. Typically, events can be classified into first, second, third, and fourth quartiles, indicating the portion of the duration where the maximum rainfall average intensity occurred. To compare with the original Huff curves, we classify storms with durations within 0–2 h, 2 h - 6 h, 6 h - 12 h, and > 12 h as the first, second, third, and fourth quartile.

3 Results

The descriptive sample analysis used to derive the rainfall temporal distributions is presented in Fig. 3. Most of the observed events have durations smaller than 5 h, with volumes of approximately 11 mm, on average. The empirical copula-based cumulative hyetographs are presented in Fig. 4. This figure is discretized into 1st, 2nd, 3rd, and 4th quartile rainfall distributions. Most of the events occurred in the 1st and 3rd quartile.

Rainfall maximum intensities and volumes are discretized for each distribution and duration, detailed in Table 2. The largest 15-minute intensities are sourced from the ABM. Noticeably, it is observed that the maximum rainfall intensities are consistently smaller for the Huff hyetographs compared to both Observed and ABM despite having the same rainfall volume.

The results presented in Fig. 6 show human-instability risk areas, flooded areas with depths larger than 0.5 m, areas with velocities larger than 2 $m \cdot s^{-1}$ and areas with infiltration larger than 80 mm in the Bellandur catchment for different rainfall temporal distributions and durations. The critical combination of rainfall temporal distribution and duration was identified as between the 6 and 12-h rainfall duration using the observed rainfall temporal distribution. Herein we assume the 6-h as the critical duration due to producing overall higher values for all rainfall distributions. For this duration, human instability hazard area of 6.74 km^2 are expected considering the observed rainfall distribution pattern, as shown in Fig. 6a. In particular, the duration of the critical rainfall

Table 2 Summary of events tested with maximum intensities given in 15-min intervals, where subscripts ABM = Alternated Blocks Method, H = Huff Method, and OBS = Observed 50% percentile

Rainfall duration [h]	i^{ABM}_{max} [$mm \cdot h^{-1}$]	i^{H}_{max} [$mm \cdot h^{-1}$]	i^{OBS}_{max} [$mm \cdot h^{-1}$]	Rainfall volume [mm]
2	174	130	49	87
6	174	42	38	125
12	174	26	24	157
24	174	16	19	197
48	174	11	20	248

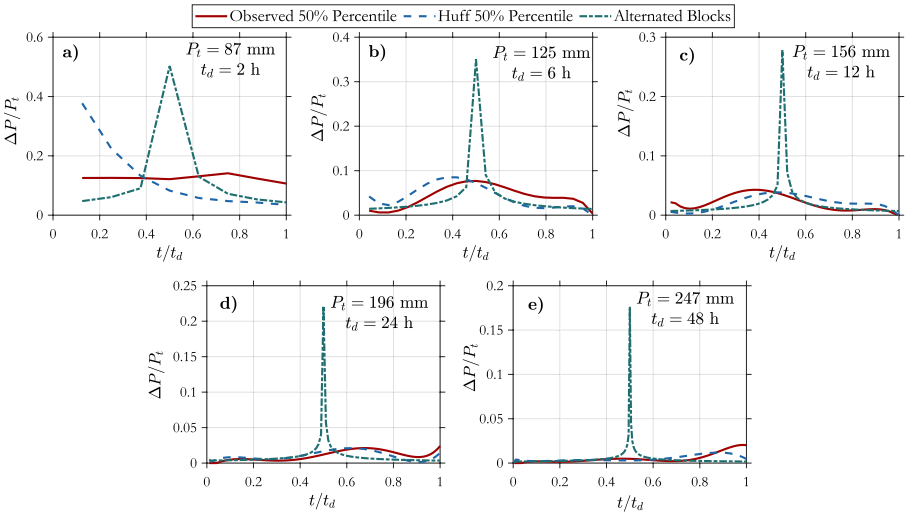

Fig. 5 Median rainfall temporal distribution for 2 (**a**), 6 (**b**), 12 (**c**), 24 (**d**), and 48 h. All charts are designed with 15-min rainfall resolution and normalized by the rainfall duration t_d. Incremental 15-min rainfall ΔP is normalized by the total precipitation (P_t)

duration was 24 h for the ABM method (12.33 km^2) and 2 h for the Huff rainfall temporal distribution (7.06 km^2). The normalized data-driven rainfall distribution compared to Huff and Alternated Blocks Method is presented in Fig. 5.

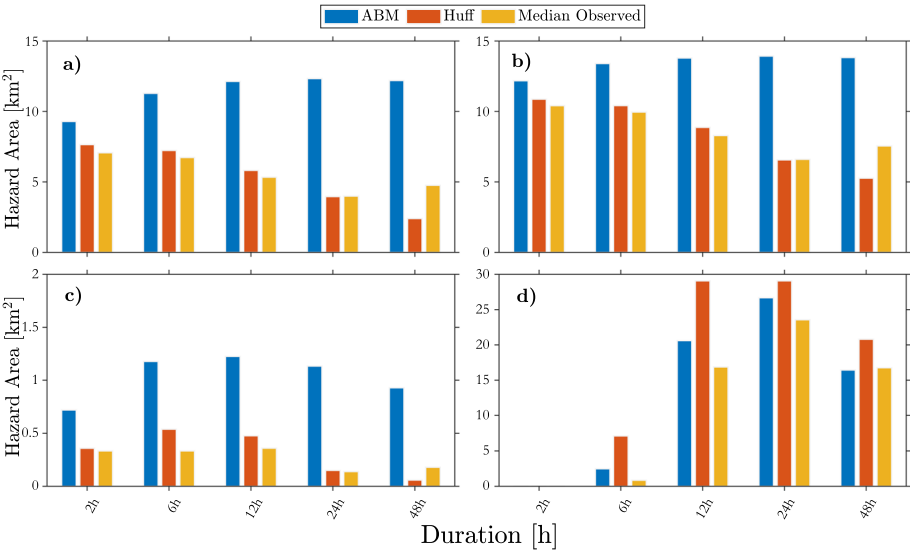

Fig. 6 Hazard areas in terms of human instability, maximum flow velocity, water depths, and infiltrated depths. Part **a** illustrates the overall areas prone to human instability, calculated by accounting for flood hydrodynamics and ground friction. Part **b** represents areas exceeding flow velocities greater than 2 m · s^{-1}. Cumulative areas surpassing flood depths of 0.5 m are shown in Part (**c**), while Part **d** displays total areas exceeding 89 mm of soil infiltration, representing the 10-yr, 6-h, storm volume

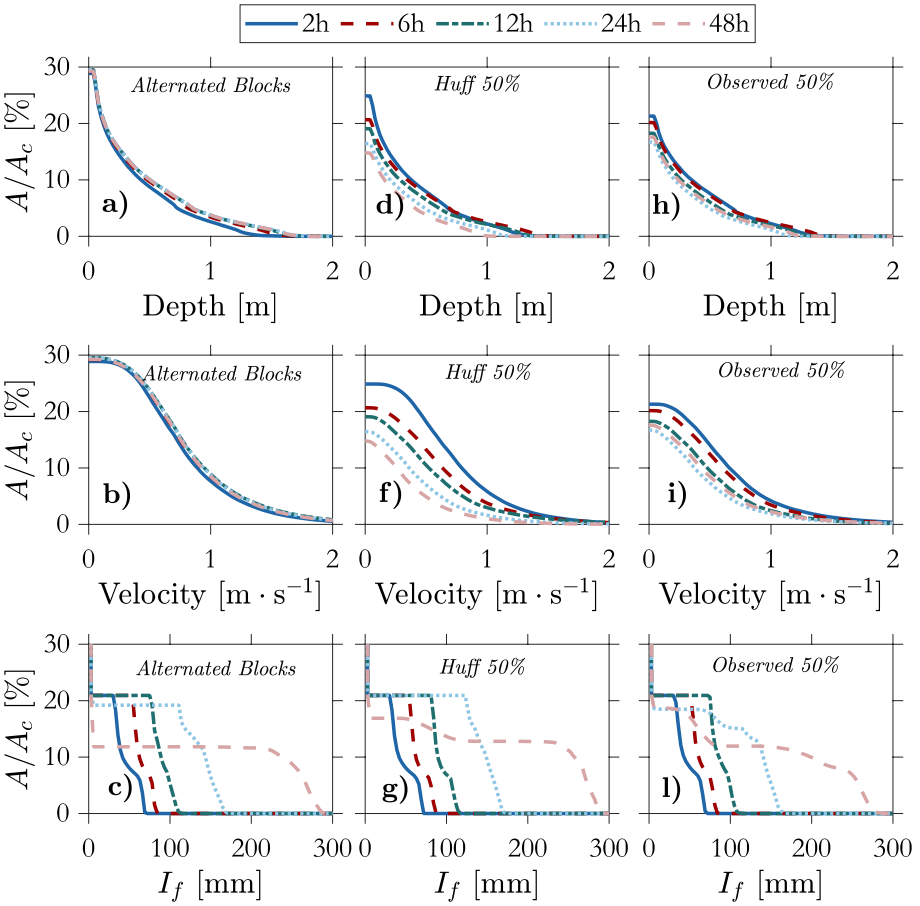

Fig. 7 Normalized spatial analysis of flood depths, velocity, and infiltrated depth, where **a–c** are results for the ABM, **d–f** are for the Huff rainfall temporal distributions, and **g–i** are median observed distribution. Results are plotted for each rainfall duration tested. Flooded areas are normalized by the catchment area $A_c = 131.37$ km^2. I_f is the cumulative infiltration depth

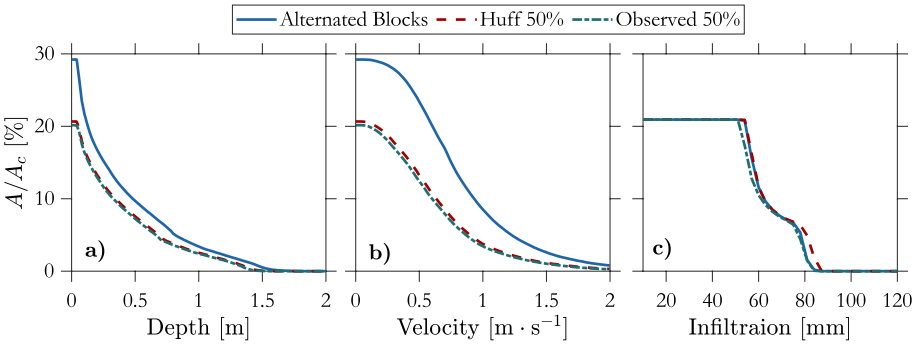

Fig. 8 Effect of different hazard areas for the critical duration of 6-h for different hazards: **a** is for the maximum flow velocity **b** is for the flow velocity, and **c** is for the infiltrated depth

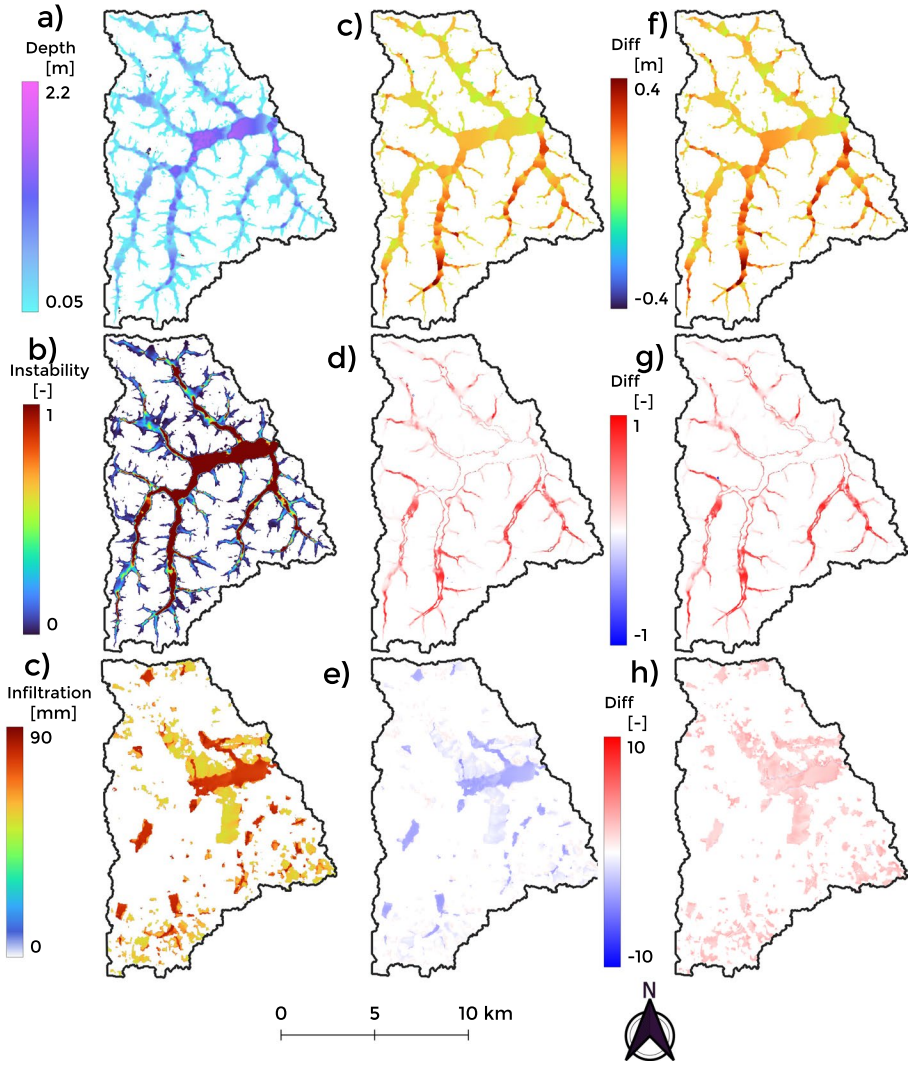

Fig. 9 Comparison between the Alternated Blocks Method results (**a**)–(**c**), to Huff (**c**)–(**e**), and to the Observed Rainfall Temporal Distribution. Parts (**a**)–(**c**) show water depths, instability hazard f_r [Eq. (7)], and infiltration values for the ABM method, respectively. Parts (**c**)–(**e**) show the difference between maps of (**a**)–(**c**) with Huff distribution modeled results. Similarly, parts **f** to **h** show the difference between ABM and the observed rainfall distribution modeled results. All results are shown, assuming a critical rainfall duration of 6-h

The critical duration and temporal distribution for flooded areas with depths larger than 0.5 m is, as opposed to the aforementioned hazard metrics, is the ABM with 12-h of rainfall duration, as observed in Fig. 6c. The ABM method consistency produced hazard flood areas 2–5 larger than the other rainfall distribution methods.

Part (c) of this figure shows the areas exceeding 89 mm of infiltration. Regarding these areas (commonly found in regions with high flow accumulation and pervious

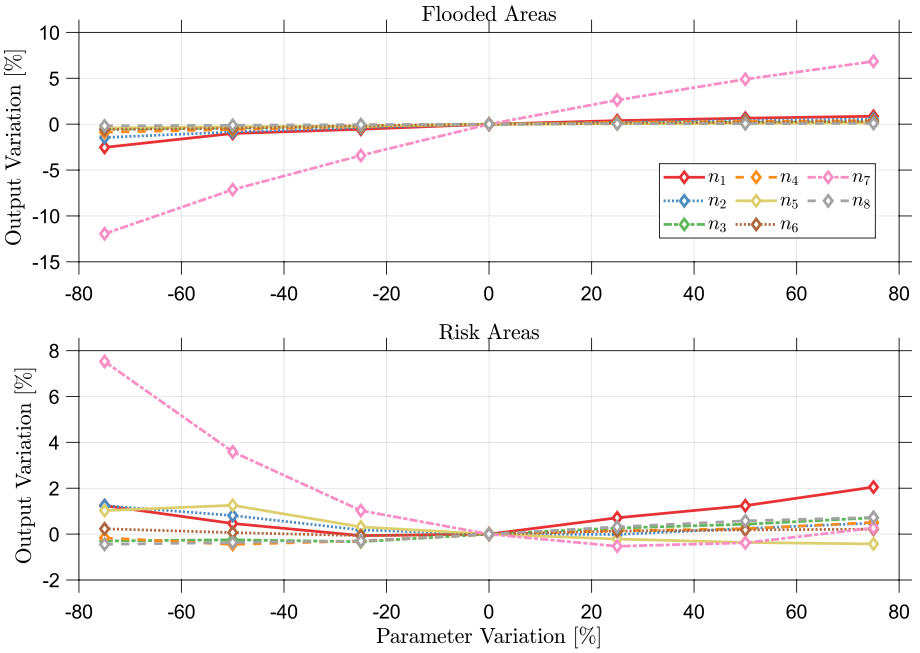

Fig. 10 One-at-the-time sensitivity analysis on Manning's roughness coefficient for the 12-h observed hyetograph with a 100-yr return period, where 1 = water, 2 = Trees, 3 = Flooded Vegetation, 4 = Crops, 5 = Shrub/Scrub, 7 = Built Areas, and 8 = Bare Ground

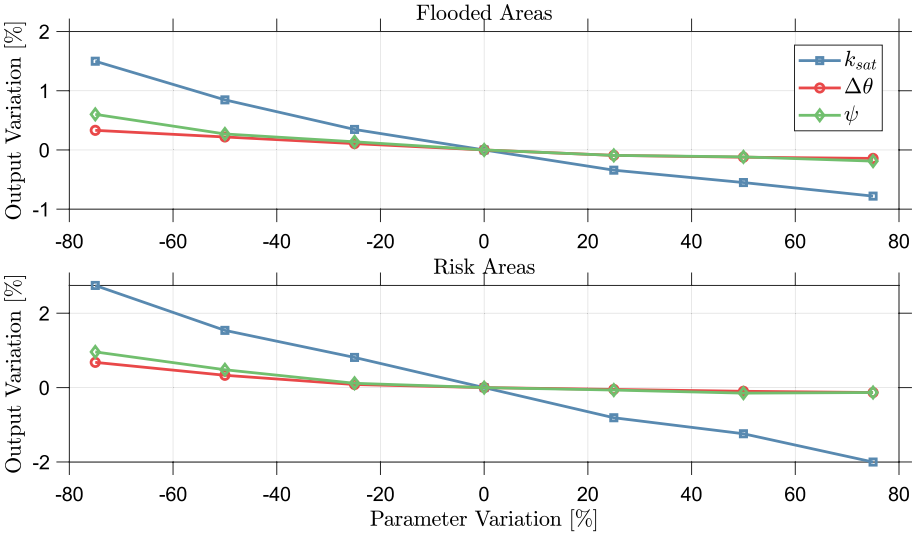

Fig. 11 One-at-the-time sensitivity analysis on Green-Ampt parameters for the infiltration model for the 12-h observed hyetograph with a 100-yr return period, where **a** are the sensitivity in Flood Areas and **b** in human instability areas in terms of the saturated hydraulic conductivity [k_{sat}], moisture deficit ($\Delta\theta$), and suction head [ψ]

areas), the Huff rainfall temporal distribution, due to its smoother spread, led to more infiltration, as evidenced in Fig. 6d. A trending peak of infiltration occurs for all methods within 12–24 h.

The results of the previous analysis are limited by the definition of the thresholds for water depth, velocity, and infiltration. For instance, one can classify a risk area if the water depth exceeds 15 cm or the flow velocity exceeds 1 $m \cdot s^{-1}$. Since this metric is subjective and may be defined by local regulation constraints that define risk thresholds, we assess the sensitivity of the extent areas where this threshold is surpassed in terms of depths, velocities, and infiltrated depths. Results of Fig. 7 show a hypsometric analysis of these variables for each rainfall duration and distribution. While the 48-hour duration is the one that produces that larger extent areas for the ABM in terms of depths and velocities (see Fig. 7a–b), it is the least critical for the Observed and Huff distributions (see Fig. 7d–e and g–h). This result shows the effect of rainfall temporal distribution variability in terms of flood characteristics.

Assuming a 6-hour duration as the critical rainfall duration, Fig. 8 illustrates the sensitivity of the flood hazard threshold for water depth, flow velocity, and infiltrated depth.

To illustrate the effects of not choosing a critical rainfall temporal distribution method, we compare the results for a 6-h duration of the observed rainfall and Huff curves, as presented in Fig. 9. The results presented in Fig. 8 can be seen spatially from the maps presented in Fig. 9. In particular, similar flooded areas and areas with human instability are expected for the median observed rainfall and original Huff temporal distribution. This result is also supported by the similar rainfall distribution trends shown in Fig. 5.

The results presented in Figs. 7 and 8 can be influenced by the choice of the model parameters presented in Table 1, since no observed discharges were available to perform a proper model calibration. Therefore, a sensitivity analysis would allow one to assess the associated uncertainty effects in the calculations and quantify the impacts of retrofitting the catchment with LIDs or by increasing urbanized areas. The one-at-the-time sensitivity analysis of the hydrodynamic and soil parameters is presented in Figs. 10 and 11, respectively.

4 Discussion

Results of Fig. 6 reveal discrepancies between the critical rainfall duration due to several non-linear factors, such as the infiltration modeling. The figure also highlights that the Huff hyetograph is less critical compared to ABM in line with findings from other studies (Balbastre-Soldevila et al 2019; Pan et al 2017; Na and Yoo 2018). The observed rainfall distribution was less critical than Huff and ABM methods, consistently resulting in smaller hazard areas with results closer to the Huff distribution. Rainfall temporal distribution is one of the governing factors of flood characteristics in urban environments (Li et al 2021) and accurate rainfall temporal resolution is essential to capture flood dynamics such as accurate time to peak and peak discharge (Lyu et al 2018).

However, the analysis does not account for flood exposure in human risk instability (Dai et al 2020). Human risk instability areas were calculated based on the maximum drag forces surpassing available friction without considering the duration where this exposure is effective. While exposure duration impacts human flood resistance, an alternative approach

calculating instability risk multiplied by the duration of occurrence falls beyond the scope of this article but could offer insights into areas with varying levels of hazard exposure.

The analysis of maximum velocities in Fig. 6b indicates consistently lower values for Huff across all tested durations compared to ABM. As expected, a strong correlation between human instability areas and maximum velocities is observed. Although the velocity estimations presented in this paper allowed the quantification of the human-instability hazard, the relatively coarse grid resolution is a limitation for properly estimating flood velocities. Recent studies the using sub-grid approach that use depth-varied hydraulic properties to propagate flood in the domain is an important alternative (Nithila Devi and Kuiry 2024); however, they require underlying high-resolution terrain models typically derived by LiDAR to obtain hydraulic properties tables for each coarse grid cell based on sub-grid data, which is unavailable in most parts of developing countries.

The ABM appears to be overall more critical as shown in Fig. 6c. Part (c) of this figure shows the areas exceeding 89 mm of infiltration. This result indicates that larger flood extents do not necessarily mean larger areas with a risk of human instability or relatively high flood velocities. It is noted that the flooded areas are 5–10 times larger than the areas of instability risk by comparing Fig. 6a with Fig. 6c. This is because some areas are natural reservoirs, and floodplains with high resistance exist within the catchment, leading to relatively low flow velocities and smaller drag forces while still getting flooded.

Regarding the infiltration analysis, areas with large infiltrated depths could be viewed as a positive metric for aquifer recharge (Mooers et al 2018); however, they can pose a flood hazard by potentially reducing the infiltration capacity for incoming storms.

For example, assuming a requirement for a 100-year return period analysis (i.e., typically required in flood hazard studies), and utilizing the Huff hyetograph for a 12-hour rainfall duration (wrongly identified as the critical duration in this analysis) would result in significantly smaller risk areas with human instability. Specifically, these areas would be 42% smaller compared to the ABM and 6% larger than the observed rainfall distribution. This holds notable implications, as insurance plans and the definition of risk areas for urban zoning often rely on delineating flood hazard areas. Opting for a noncritical rainfall temporal distribution could potentially indicate nearly 50% fewer areas at risk of flooding if ABM is a requirement for delineating flood areas. The careful choice of rainfall temporal distribution and duration used in the flood hazard analysis must be chosen (Bezak et al 2018).

The analysis of the results of Fig. 8 can be used to establish varying levels of protection for flood insurance plans, among other applications. Although the analysis in this paper shows a simple heuristic way to determine a critical rainfall duration, these results are catchment-dependent and vary according to the physiographic properties of the catchment, local rainfall pattern, and urban infrastructure.

In Fig. 8, it is evident that for relatively high velocities, the hazard areas are 5–6 times larger for the ABM compared to the Huff and observed distribution. Part (c) shows that infiltration distribution is similar comparing Huff and ABM, with Huff favoring more areas with infiltration.

As anticipated, the Built Areas and Water land use/land cover (LULC) classifications exhibit the highest sensitivity, given the significant urbanized areas and water bodies within the catchment (see Fig. 10). The surface roughness coefficient demonstrates more pronounced elasticity to parameter reduction than to parameter increase. Even with a 20% uncertainty range in roughness coefficients, errors in flood areas and human instability areas remain below 5%, indicating a relatively low level of uncertainty associated with the parameters and, consequently, with the previously provided estimations of flood hazard.

Nevertheless, for variations exceeding 20% in the parameter estimation, the sensitivity of human instability areas becomes more pronounced. Notably, an intriguing observation is that elevating the Manning's roughness coefficient (n) results in an increase in flooded areas but induces a more substantial reduction in human instability areas, as depicted in Fig. 10a, b. Consequently, retrofitting urban areas with green infrastructure may expand flood-prone regions, yet it concurrently diminishes risks of human instability to a greater extent. This suggests that green infrastructure could effectively mitigate human instability and that only flooded areas might be an incomplete metric for assessing flood hazards.

This finding holds significance for flood insurance programs exclusively reliant on flooded areas, as an increase in flooded areas does not necessarily correlate with a reduction in human instability areas. Integrating human instability maps into formulating flood insurance policies could offer a more comprehensive perspective, providing a more accurate estimation of the real impacts of floods on humans.

The flooded area extents, as indicated in Fig. 11, exhibited relatively low sensitivity to Green-Ampt soil properties, especially due to the relatively smaller pervious areas compared to the impervious areas. Conversely, soil parameters are crucial in influencing variations in areas with risks of human instability. Increasing the saturated hydraulic conductivity (k_{sat}) by 80%, from 5 to 9 $mm \cdot h^{-1}$ in pervious areas, has the potential to reduce areas of human instability by 10%.

Implementing engineering strategies such as building infiltration techniques or increasing macropores in pervious areas could achieve this reduction (Gomes Jr et al 2023). While altering saturated hydraulic conductivity might pose challenges, it is a straightforward proxy parameter for assessing the impacts of increased infiltration in the catchment. This result, coupled with an increase in Manning's roughness coefficient (n), underscores the advantages of implementing green infrastructure retrofits in the catchment, leading to a reduction in areas with flood hazards (McClymont et al 2020; Borah et al 2023).

5 Conclusions

A flood inundation model, incorporating a human instability module and employing both synthetic and observed rainfall temporal distribution methods, was developed and implemented in the Bellandur catchment in Bangalore, India. The study investigated the impact of various rainfall temporal distributions on flood characteristics, including inundation extents, depths, velocities, and soil infiltration. This analysis aimed to assess the uncertainty associated with assuming an a priori synthetic rainfall temporal distribution for flood inundation mapping and modeling and the potential impacts in flood hazard assessment. The discrepancies can be even larger if rainfall temporal distribution is not critical, as well as rainfall duration. The systematic method to evaluate the critical rainfall temporal distribution and duration presented in this paper can be applied to produce critical flood maps for a given return period, which is typically the only criteria established by local flood regulations.

The preselection of a synthetic rainfall temporal distribution for flood mapping and modeling, without evaluating the sensitivity of various synthetic rainfall temporal distribution methods or incorporating observed fitted rainfall temporal distributions, may result in a considerable uncertainty, potentially leading to a misrepresentation of up to 45% smaller areas with flood hazards related to human instability for a 100-year flood event.

The sensitivity analysis of the hydrodynamic and hydrologic parameters of the catchment indicates a relatively lower degree of sensitivity in flood areas and human instability areas (i.e., smaller than 20% for a variation of 80% in all parameters), allowing the use of

the model for preliminary assessment without formal calibration that would require inaccessible stream flow and spatially distributed rainfall. This indicates a scenario where the application of 2D hydrologic-hydrodynamic modeling can generate useful information for catchments with a lack of observed hydrological data but is prone to floods.

In the particular case of highly urbanized catchments as Bangalore, having soils with higher infiltration capacity produces little effect in mitigating flood effects for a 100-yr event. However, if the terrain roughness of the impervious areas is changed, it is possible to achieve 5–10 % variations in flooded and risk areas. Increasing terrain roughness increases flooded areas but reduces instability areas and can be viewed hence as a positive metric. Therefore, a combined metric of flooding areas with human instability areas can be a more complete metric to aid flood risk assessment.

The automatic one-at-a-time sensitivity algorithms, developed and implemented in the HydroPol2D model in this study, serve as a valuable tool for comprehending the consequences of retrofitting the catchment with various low-impact development scenarios. Additionally, HydroPol2D allows for straightforward sensitivity analysis of different rainfall temporal distributions, durations, and return periods. Replicating the methods established in this paper with other ungauged or poorly-gauged catchments provides an alternative for furnishing valuable information in areas lacking data but facing potential unprecedented floods in the future due to urbanization and climate change. Applying this strategy to other highly urbanized and flood-prone catchments is justified.

The 100-yr events tested in this paper are conditioned to the exceedance probability of rainfall volume for a given duration, given the occurrence probability of the rainfall temporal distribution. We used the 50th percentile as the representative temporal distribution for the analysis; however, a monte-carlo analysis evaluating the combined probability of the rainfall volume and temporal distribution can be analyzed to investigate the critical temporal distribution based on the observed data. A practical ensemble analysis can be done by using each 10th percentile of the observed rainfall distributions to investigate the effect of possible different observed storms in the flood hazard assessment. Future studies can also incorporate the spatial behavior of rainfall and its impacts on human instability metrics, especially because the center of the rainfall can influence the total potential energy, which ultimately would convert to larger flood velocities downstream of the catchment. The effect of initial moisture content in the simulation and the analysis of coupled effects combining rainfall temporal distribution methods and increasing rainfall rates due to climate change can also be further investigated.

The results of this paper make clear the case that only specifying the return period is a poor local regulation criterion to be used for flood mapping. The non-linear dynamics of infiltration and flood routing coupled with the rainfall temporal distribution characteristics make the preselection of rainfall duration and temporal distribution complex without identifying the critical combination. Several simulations must be performed with different durations, synthetic, and data-driven rainfall temporal distributions to identify the critical durations for a given flood hazard.

Electronic supplementary material The online version of this article (https://doi.org/10.1007/s11069-025-07186-3) contains supplementary material, which is available to authorized users.

Acknowledgements The authors appreciate the support of CAPES Ph.D Scholarship and the PPGSHS PROEX Graduate Program. E.M.M. thanks the projects: “OUR EYES” (glObal changes and sUstainable development with wateR-Energy viabilitY and economic Solvency, FAPESP # 22/07521-5) and “DREAMS” (flash DRought Event evolution chAracteristics and the response MechaniSm to climate change, FAPESP # 22/08468-0).

Funding CAPES - Award 88887.663281/2022-00.

Declarations

Conflict of interest The authors have no relevant financial or non-financial interests to disclose.

Ethical approval This material is the authors' own original work, which has not been previously published elsewhere. The paper is not currently being considered for publication elsewhere. The paper reflects the authors' own research and analysis in a truthful and complete manner. The paper properly credits the meaningful contributions of co-authors and co-researchers. The results are appropriately placed in the context of prior and existing research. All sources used are properly disclosed (correct citation). Literally copying of text must be indicated as such by using quotation marks and giving proper references. All authors have been personally and actively involved in substantial work leading to the paper and will take public responsibility for its content.

References

Avinash S (2013) Flood related disasters: concerned to urban flooding in bangalore, india. Education 2020

Avinash S, Prasad KL, Reddy G et al (2018) Urban flood forecast system-a case study of bangalore, india. Univ Rev

Balbastre-Soldevila R, García-Bartual R, Andrés-Doménech I (2019) A comparison of design storms for urban drainage system applications. Water 11(4):757

Bates PD, Horritt MS, Fewtrell TJ (2010) A simple inertial formulation of the shallow water equations for efficient two-dimensional flood inundation modelling. J Hydrol 387(1–2):33–45

Bezak N, Šraj M, Rusjan S et al (2018) Impact of the rainfall duration and temporal rainfall distribution defined using the huff curves on the hydraulic flood modelling results. Geosciences 8(2):69

Bhagat RB (2011) Emerging pattern of urbanisation in india. Econ Pol Wkly 46(34):10–12

Borah A, Bardhan R, Bhatia U (2023) Protecting heritage: insights into effective flood management using green infrastructure in a highly urbanized environment. Int J Disaster Risk Reduct 98:104075

Breinl K, Lun D, Müller-Thomy H et al (2021) Understanding the relationship between rainfall and flood probabilities through combined intensity-duration-frequency analysis. J Hydrol 602:126759

Brown CF, Brumby SP, Guzder-Williams B et al (2022) Dynamic world, near real-time global 10 m land use land cover mapping. Scientific Data 9(1):251

Brunner GW (2016) Hec-ras river analysis system: hydraulic reference manual, version 5.0. US Army Corps of Engineers–Hydrologic Engineering Center 547

Chandrashekar J, Babu L, Somashekar R (2003) Impact of urbanization on bellandur lake, bangalore- a case study. J Environ Biol 24(3):223–227

Chen G, Hou J, Hu Y et al (2023) Simulated investigation on the impact of spatial-temporal variability of rainstorms on flash flood discharge process in small watershed. Water Resour Manage 37(3):995–1011

Cheng T, Xu Z, Yang H et al (2020) Analysis of effect of rainfall patterns on urban flood process by coupled hydrological and hydrodynamic modeling. J Hydrol Eng 25(1):04019061

Conrad O, Bechtel B, Bock M et al (2015) System for automated geoscientific analyses (saga) v. 2. 1. 4. Geosci Model Dev 8(7):1991–2007

Cristiano E, ten Veldhuis MC, Van De Giesen N (2017) Spatial and temporal variability of rainfall and their effects on hydrological response in urban areas-a review. Hydrol Earth Syst Sci 21(7):3859–3878

Dai Q, Zhu X, Zhuo L et al (2020) A hazard-human coupled model (hazardcm) to assess city dynamic exposure to rainfall-triggered natural hazards. Environ Model & Softw 127:104684

De U, Singh G, Rase D (2013) Urban flooding in recent decades in four mega cities of india. J Ind Geophys Union 17(2):153–165

De Almeida GA, Bates P (2013) Applicability of the local inertial approximation of the shallow water equations to flood modeling. Water Resour Res 49(8):4833–4844

De Paiva RCD, Buarque DC, Collischonn W et al (2013) Large-scale hydrologic and hydrodynamic modeling of the amazon river basin. Water Resour Res 49(3):1226–1243

Dottori F, Alfieri L, Bianchi A et al (2022) A new dataset of river flood hazard maps for europe and the mediterranean basin. Earth System Science Data 14(4):1549–1569

Gomes MN, Do Lago CAF, Rápalo LMC et al (2023) Hydropol2d - distributed hydrodynamic and water quality model: challenges and opportunities in poorly-gauged catchments. J Hydrol 625:129982. https://doi.org/10.1016/j.jhydrol.2023.129982

Gomes MN Jr, Giacomoni MH, de Macedo MB et al (2023) A modeling framework for bioretention analysis: assessing the hydrologic performance under system uncertainty. J Hydrol Eng 28(9):04023025
Gomes Jr MN, Castro MA, Castillo LM et al (2024) Spatio-temporal performance of 2d local inertial hydrodynamic models for urban drainage and dam-break applications. arXiv preprint arXiv:2410.09325
Green WH, Ampt GA (1911) Studies on soil phyics. J Agric Sci 4(1):1–24
Huang X, Wang C (2020) Estimates of exposure to the 100-year floods in the conterminous united states using national building footprints. Int J Disaster Risk Reduct 50:101731
Huber WC, Rossman LA, Dickinson RE (2005) Epa storm water management model, swmm5. Watershed models 338:359
Huff FA (1967) Time distribution of rainfall in heavy storms. Water Resour Res 3(4):1007–1019
Jonkman S, Penning-Rowsell E (2008) Human instability in flood flows 1. JAWRA J Am Water Resour Assoc 44(5):1208–1218
Kang M, Goo J, Song I et al (2013) Estimating design floods based on the critical storm duration for small watersheds. J Hydro-Environ Res 7(3):209–218
Kc S, Wurzer M, Speringer M et al (2018) Future population and human capital in heterogeneous india. Proc Natl Acad Sci 115(33):8328–8333
Krvavica N, Rubinić J (2020) Evaluation of design storms and critical rainfall durations for flood prediction in partially urbanized catchments. Water 12(7):2044
Kvočka D, Falconer RA, Bray M (2016) Flood hazard assessment for extreme flood events. Nat Hazards 84:1569–1599
Do Lago CA, Giacomoni MH, Bentivoglio R et al (2023) Generalizing rapid flood predictions to unseen urban catchments with conditional generative adversarial networks. J Hydrol 618:129276
Lazzarin T, Viero DP, Molinari D et al (2022) Flood damage functions based on a single physics-and data-based impact parameter that jointly accounts for water depth and velocity. J Hydrol 607:127485
Lazzarin T, Chen AS, Viero DP (2024) Beyond flood hazard. mapping the loss probability of pedestrians to improve risk estimation and communication. Sci Total Environ 912:168718
Li T, Lee G, Kim G (2021) Case study of urban flood inundation-impact of temporal variability in rainfall events. Water 13(23):3438
Lyu H, Ni G, Cao X et al (2018) Effect of temporal resolution of rainfall on simulation of urban flood processes. Water 10(7):880
Batalini de Macedo M, Gomes Júnior MN, Jochelavicius V et al (2022) Modular design of bioretention systems for sustainable stormwater management under drivers of urbanization and climate change. Sustainability 14(11):6799
Mani P, Chatterjee C, Kumar R (2014) Flood hazard assessment with multiparameter approach derived from coupled 1d and 2d hydrodynamic flow model. Nat Hazards 70:1553–1574
McClymont K, Cunha DGF, Maidment C et al (2020) Towards urban resilience through sustainable drainage systems: A multi-objective optimisation problem. J Environ Manage 275:111173
Mei C, Liu J, Wang H et al (2020) Urban flood inundation and damage assessment based on numerical simulations of design rainstorms with different characteristics. Sci China Technol Sci 63:2292–2304
Membele GM, Naidu M, Mutanga O (2022) Examining flood vulnerability mapping approaches in developing countries: a scoping review. Int J Disaster Risk Reduct 69:102766
Mooers EW, Jamieson RC, Hayward JL et al (2018) Low-impact development effects on aquifer recharge using coupled surface and groundwater models. J Hydrol Eng 23(9):04018040
Mosavi A, Ozturk P, Kw Chau (2018) Flood prediction using machine learning models: literature review. Water 10(11):1536
Na W, Yoo C (2018) Evaluation of rainfall temporal distribution models with annual maximum rainfall events in seoul, korea. Water 10(10):1468
Nations U (2022) World population prospects 2019. https://population.un.org/dataportal/data/indicators/49/locations/356/start/1990/end/2024/line/linetimeplot?df=87204aca-997a-4ae9-a731-b34abfa99773
Nithila Devi N, Kuiry SN (2024) A novel local-inertial formulation representing subgrid scale topographic effects for urban flood simulation. Water Resour Res 60(5):e2023WR035334
Pan C, Wang X, Liu L et al (2017) Improvement to the huff curve for design storms and urban flooding simulations in guangzhou, china. Water 9(6):411
Pena F, Obeysekera J, Jane R et al (2023) Investigating compound flooding in a low elevation coastal karst environment using multivariate statistical and 2d hydrodynamic modeling. Weather Clim Extrem 39:100534
Pregnolato M, West C, Evans B et al (2024) Using multi-stakeholder causal mapping to explore priorities for infrastructure resilience to flooding. Int J Disaster Risk Reduct 101:104189
Ramachandra T, Aithal BH (2019) Bangalore. The Wiley Blackwell Encyclopedia of Urban and Regional Studies pp 1–21

Ramachandra T, Mujumdar PP (2009) Urban floods: case study of bangalore. Disaster Dev 3(2):1–98
Restrepo-Posada PJ, Eagleson PS (1982) Identification of independent rainstorms. J Hydrol 55(1–4):303–319
Roldán-Valcarce A, Jato-Espino D, Manchado C et al (2023) Vulnerability to urban flooding assessed based on spatial demographic, socio-economic and infrastructure inequalities. Int J Disaster Risk Reduct 95:103894
Rossman LA (2010) Storm water management model user's manual, version 5.0. National Risk Management Research Laboratory, Office of Research and ..
Schwanghart W, Scherler D (2014) Topotoolbox 2-matlab-based software for topographic analysis and modeling in earth surface sciences. Earth Surf Dyn 2(1):1–7
Sridharan B, Gurivindapalli D, Kuiry SN et al (2020) Explicit expression of weighting factor for improved estimation of numerical flux in local inertial models. Water Resour Res 56(7):e2020WR027357
Te Chow V (1959) Open channel hydraulics
Teng J, Jakeman AJ, Vaze J et al (2017) Flood inundation modelling: a review of methods, recent advances and uncertainty analysis. Environ Model & Softw 90:201–216
Westra S, Fowler HJ, Evans JP et al (2014) Future changes to the intensity and frequency of short-duration extreme rainfall. Rev Geophys 52(3):522–555
Yuan W, Tu X, Su C et al (2021) Research on the critical rainfall of flash floods in small watersheds based on the design of characteristic rainfall patterns. Water Resour Manage 35:3297–3319
Zare N, Maknoon R et al (2024) Urban flood resilience assessment & stormwater management (case study: District 6 of tehran). Int J Disaster Risk Reduct 102:104280
Zhu Z, Wright DB, Yu G (2018) The impact of rainfall space-time structure in flood frequency analysis. Water Resour Res 54(11):8983–8998

Authors and Affiliations

Marcus N. Gomes Jr.[1,2,3] · Vijay Jalihal[4] · Maria Castro[3] · Eduardo M. Mendiondo[3]

✉ Marcus N. Gomes Jr.
marcusnobrega@arizona.edu

Vijay Jalihal
vijay.jalihal@vanderbilt.edu

Maria Castro
mariaandrade@arizona.edu

Eduardo M. Mendiondo
emm@usp.sc

[1] Department of Hydraulic Engineering and Sanitation, Sao Carlos School of Engineering, University of Sao Paulo, Rua Trabalhador Sao Carlense, Sao Carlos, Sao Paulo 13566-590, Brazil

[2] College of Engineering and Integrated Design, School of Civil Environmental Engineering and Construction Management, The University of Texas at San Antonio, One UTSA Circle, San Antonio, TX 78249, USA

[3] Department of Hydrology and Atmospheric Sciences, University of Arizona, James E. Rogers Way, Tucson, AZ 85719, USA

[4] Department of Civil and Environmental Engineering, Vanderbilt University, Jacobs Hall, TN, Nashville 37235, USA